ARTICLE   OPEN

On-chip parallel processing of quantum frequency comb

Liang Zhang[1], Chaohan Cui[1], Jianchang Yan[2], Yanan Guo[2], Junxi Wang[2] and Linran Fan [1✉]

The frequency degree of freedom of optical photons has been recently explored for efficient quantum information processing. Significant reduction in hardware resources and enhancement of quantum functions can be expected by leveraging the large number of frequency modes. Here, we develop an integrated photonic platform for the generation and parallel processing of quantum frequency combs (QFCs). Cavity-enhanced parametric down-conversion with Sagnac configuration is implemented to generate QFCs with identical spectral distributions. On-chip quantum interference of different frequency modes is simultaneously realized with the same photonic circuit. High interference visibility is maintained across all frequency modes with the identical circuit setting. This enables the on-chip reconfiguration of QFCs. By deterministically separating QFCs without spectral filtering, we further demonstrate high-dimensional Hong-Ou-Mandel effect. Our work provides the critical step for the efficient implementation of quantum information processing with integrated photonics using the frequency degree of freedom.

INTRODUCTION

The generalization of two-level quantum systems to high dimensions provides the capability to verify quantum theories with stronger criteria, perform quantum computing with better error resilience, and conduct quantum communications with higher capacity and noise robustness[1–3]. Optical photons are the ideal candidate for high-dimensional encoding[4]. Various degrees of freedom including path[5], orbital angular momentum[6,7], frequency[8–12], spatial[13–15], and temporal modes[16,17], have been used for high-dimensional photonic entanglement generation. Among different degrees of freedom, frequency is particularly promising for the on-chip implementation of high-dimensional quantum information processing, as it does not require challenging integrated photonic components such as ultra-long delay lines and highly multimodal waveguides in other approaches[9–12].

Biphoton quantum frequency combs (QFCs), the superposition of signal-idler photon pairs in discrete spectral modes, have been generated on integrated platforms based on spontaneous four-wave mixing processes[9–12]. Advanced quantum functions such as quantum communications with wavelength-division multiplexing[18] and coherent superposition of multiple frequency modes[9] have been realized based on integrated QFCs. However, the operation of QFCs is typically realized with discrete components, diminishing the scalability advantage of integrated QFCs. Moreover, it is beneficial to generate integrated QFCs with the second-order nonlinearity, which can provide significantly higher power efficiency than spontaneous four-wave mixing.

Here, we demonstrate the on-chip parallel processing of QFCs based on the integrated aluminum nitride (AlN) platform. QFCs with near-identical spectral distribution are simultaneously generated with cavity-enhanced parametric down-conversion in the Sagnac configuration. We realize the parallel quantum interference of different frequency modes with the integrated phase shifter and beamsplitter. The uniform response and high interference visibility across all frequency modes allow us to deterministically separate photon pairs in QFCs without using spectral filtering, leading to the demonstration of high-dimensional Hong-Ou-Mandel effect.

RESULTS

Platform for parallel processing of QFCs

The schematic for the on-chip generation and manipulation of QFCs is shown in Fig. 1a. The pump around 775 nm wavelength is equally split, and coupled into the clockwise (CW) and counter-clockwise (CCW) directions of the integrated photonic ring cavity. The second-order ($\chi^{(2)}$) nonlinearity of AlN enables efficient parametric down-conversion inside the cavity. With the large phase matching bandwidth, photon pairs in the telecom wavelength regime are generated in the superposition of multiple cavity resonances, forming QFCs. The simultaneous generation of QFCs in CW and CCW directions of the same cavity ensures the near-identical spectral distribution[19]. Therefore, the high-dimensional interference of QFCs can maintain high visibility. The relative phase φ between QFCs can be controlled by an on-chip phase shifter. After interference at the balanced multimode interferometer, the output state can be written as

$$
|\psi_{\text{out}}\rangle = \frac{1}{\sqrt{4N+2}} \sum_{k=-N}^{N} \left[\cos\varphi (\hat{b}_k^\dagger \hat{b}_{-k}^\dagger + \hat{c}_k^\dagger \hat{c}_{-k}^\dagger) - i\sin\varphi (\hat{b}_k^\dagger \hat{c}_{-k}^\dagger + \hat{b}_{-k}^\dagger \hat{c}_k^\dagger) \right] |0\rangle
$$

(1)

where $\hat{b}^\dagger$ and $\hat{c}^\dagger$ are the creation operators for the upper and lower paths, k labels the frequency mode, and the total number of frequency modes is $2N+1$ (Supplementary Note I). The output state structure with frequency correlation in symmetric spectral modes across CW and CCW paths is illustrated in Fig. 1b.

QFC generation

The complete photonic circuit is fabricated with AlN-on-sapphire wafer. The photonic ring cavity has a radius of 60 μm with a free-spectral range (FSR) of 362 GHz (2.9 nm). The phase matching for parametric down-conversion is realized with modal dispersion engineering (Supplementary Note II)[20]. We first characterize individual QFCs with the measurement setup shown in Fig. 2a. A narrow-linewidth tunable laser is used as the pump with wavelength 777.84 nm and on-chip power 3 mW. A separate

[1]James C. Wyant College of Optical Sciences, The University of Arizona, Tucson, AZ 85721, USA. [2]Research and Development Center for Solid State Lighting, Institute of Semiconductors, Chinese Academy of Sciences, Beijing 100083, China. ✉email: lfan@optics.arizona.edu
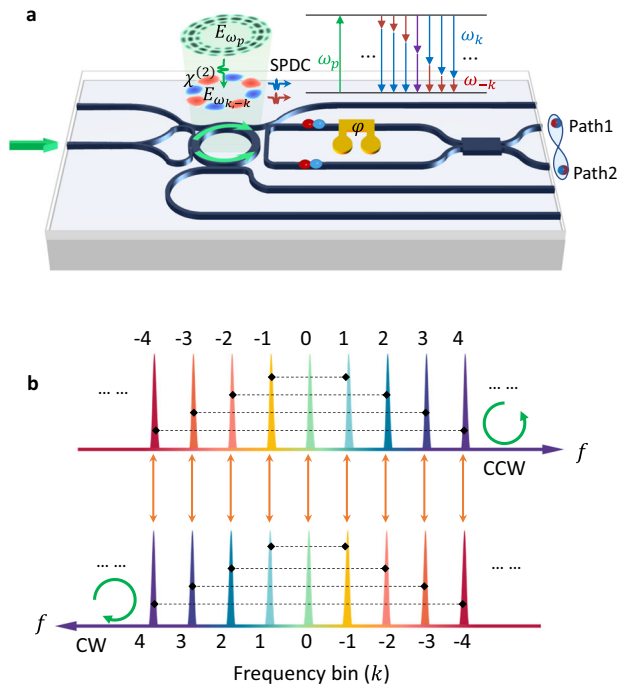
Fig. 1 Integrated platform for the parallel processing of quantum frequency combs. a Schematic to show the device layout for the parallel processing of QFCs. The continuous-wave pump (green) is coupled onto the chip, equally split with a Y-junction, and coupled into the integrated ring cavity in both CW and CCW directions. Intracavity parametric down-conversion generates frequency-entangled photon pairs across multiple cavity resonances. Output photon pairs are interfered with tunable relative phase φ on a 50/50 multimode interferometer. A separate bus waveguides is used to calibrate the device. **b** Output state structure with frequency correlation in symmetric spectral modes across CW and CCW paths.

calibration waveguide is used to extract QFCs in both CW and CCW directions. At the output, pump light is removed by longpass filters (LPFs). Narrow bandpass tunable filters (TFs) are used to select different frequency modes, and photons are detected by superconducting nanowire single photon detectors (SNSPDs). QFCs in CW and CCW directions show similar single-photon spectrums, with peak locations matching cavity resonances (Fig. 2b). The measured average coincidence rate for one resonance pair is 7 kHz, implying around 2 MHz photon pair generation rate on-chip. Then QFCs are equally split with a 50/50 beamsplitter. Two sets of filters and SNSPDs are used to measure the frequency correlation of QFCs. Strong correlation is only observed between frequency modes located symmetrically to the degenerate wavelength at 1555.68 nm (Fig. 2c, d). The coincidence-to-accidental ratio above 25 dB has been achieved for all resonance pairs. Assuming the coherent superposition of photon pairs in different resonances, the lower bound of QFCs can be obtained by the Schmidt decomposition of the frequency correlation matrix[21,22]. The Schmidt number scales linearly with the number of resonance pairs (Fig. 2f). With ten resonance pairs, the lower bound of QFCs is estimated above 9.2.

We further use self-correlation measurement in the time domain with Hanbury-Brown-Twiss setup to characterize the multi-resonance property of QFCs. The peak value of the self-correlation function at zero time delay $g^{(2)}(0)$ directly reflects the number of resonance pairs in QFCs $g^{(2)}(0) = 1 + \frac{1}{N}$ (Fig. 2e)[23–25]. A linear relation between resonance pair numbers estimated based on the self-correlation measurement and calculated based on filter bandwidth is observed (Fig. 2f).

Parallel processing of QFCs

To demonstrate the parallel processing, QFCs in CW and CCW directions are combined with an on-chip 50/50 beamsplitter. The relative phase φ between QFCs is controlled with an on-chip thermo-optic phase shifter. Four sets of filters and SNSPDs are used to measure the frequency correlation within each paths and cross different paths (Fig. 3a). The interference pattern of the coherent light through a calibration Mach-Zehnder interferometer with the same phase shifter and beamsplitter design is used as the classical reference (Fig. 3b) (Supplementary Note III). Then we measure the interference pattern of QFCs. We first isolate the degenerate resonance ($k = 0$) and measure the self-correlation of the upper path $S_{0,0}$ and the cross-correlation between the two paths $C_{0,0}$ (Fig. 3c). Both self- and cross-correlation show periods half of the classical interference with complementary count rates. In contrast to classical interference where only phase φ is obtained, a 2φ phase shift is applied to QFCs. This agrees with Eq. (1) which suggests $S_{0,0} \propto \cos^2\varphi$ and $C_{0,0} \propto \sin^2\varphi$. The quantum interference shows high visibility of $93.8 \pm 0.51\%$ without background noise subtraction. While the phase doubling in the interference pattern is a quantum effect and a signature of two-photon N00N state, it is insufficient to prove the entanglement in the path-domain, which requires projection measurements onto orthogonal basis.

Another key difference between the classical and quantum interference is the dispersion response. The interference pattern shifts depending on wavelengths in the classical case. In the quantum case, the collective phase of the photon pair determines the interference pattern, which is the fundamental principle behind nonlocal dispersion cancellation[26]. With the fixed sum frequency, the total accumulated phase for symmetric resonances ($\varphi_k + \varphi_{-k}$) stays constant, leading to the same interference pattern for different resonance pairs. We verify this by measuring the correlation between symmetric frequency modes in the same path $S_{k,-k}$ as well as in different paths $C_{k,-k}$. Interference patterns remain the same as the degenerate case and high visibility is maintained (Fig. 3f). As an example, we present the interference pattern for the fourth pair ($k = 4$) (Fig. 3d). In particular, the driving power of the phase shifter remains consistent for different resonance pairs (Fig. 3g). This enables the parallel processing of QFCs. Furthermore, we use a programmable filter to select multiple frequency bins ($k = 0$ to 4) together to perform the interference of QFCs. The interference pattern of QFCs remains the same as individual frequency modes (Fig. 3e).

The parallel processing of QFCs can be further examined through the simultaneous measurement of the correlation in both path and frequency domains. QFCs can be reconfigured to exhibit bunching, coherent superposition, and anti-bunching between the two paths by setting the phase shifter to be $\varphi = 0, \pi/4$, and $\pi/2$ respectively (Fig. 4a–c). Under the bunching condition ($\varphi = 0$), photons in QFCs are grouped into the same path. Therefore, strong correlation can be observed within each path, but only between symmetric frequency modes (Fig. 4a). Under the antibunching condition ($\varphi = \pi/2$), photons in QFCs are deterministically separated[27]. Therefore, no correlation is observed between any resonance pairs in the same path (Fig. 4c).

The capability to deterministically separate photons in QFCs allows us to demonstrate high-dimensional Hong-Ou-Mandel effect (Fig. 5a). A tunable optical delay line (ODL) is placed in one path to control the relative time delay, and a fiber polarization controller is used to match the polarization between the two paths. After interference at a balanced fiber beamsplitter, the coincidence is recorded by SNSPDs. A pair of programmable filters (PF) is used to select frequency modes. We first select only the degenerate frequency mode in both paths. The standard Hong-Ou-Mandel interference is observed with a
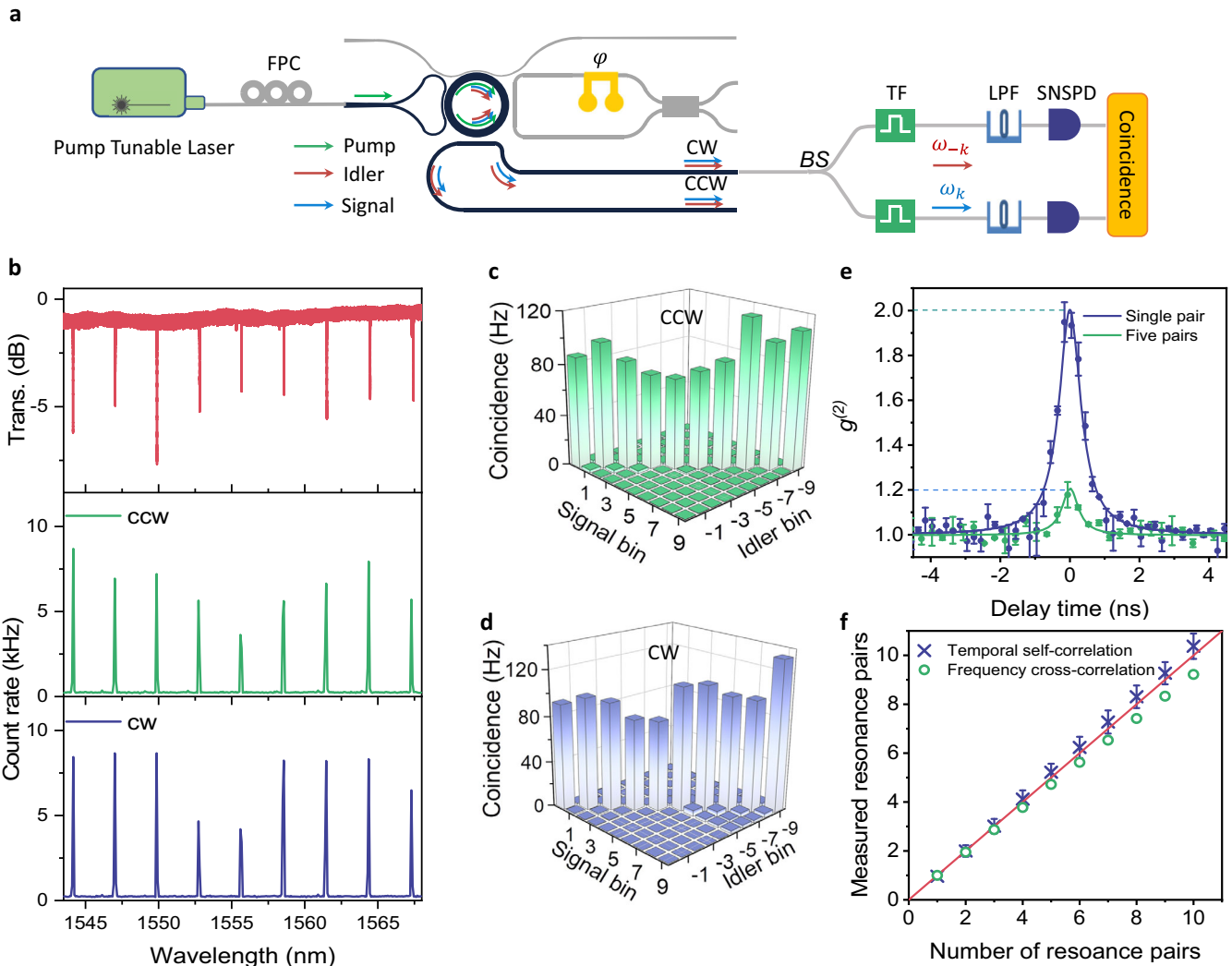
a

b

c

d

e

f

Fig. 2 Generation of quantum frequency combs. a Schematic of the measurement setup for QFC characterization. FPC fiber polarization controller, BS beamsplitter, LPF long-pass filter, SNSPD superconducting nanowire single photon detector, TF tunable filter. **b** Classical transmission spectrum (red) and off-chip single-photon spectrum of CCW (green) and CW (blue) QFCs. **c, d** Measured frequency correlation of the CW and CCW QFCs respectively without loss correction. **e** Self-correlation of photons generated from the single degenerate resonance and five resonances of CW QFC. **f** QFC resonaces pairs estimated from the temporal self-correlation measurement and the Schmidt decomposition of the frequency correlation matrix respectively. The red line is the ideal relationship between dimension and resonance pairs.

single dip at zero time delay (Fig. 5b). Visibility around $89.6 \pm 2.5\%$ is achieved without subtracting the background noise. The Hong-Ou-Mandel dip FWHM is measured around 1.67 ns, which is consistent with the resonance linewidth (623 MHz)[8]. We further program the filters to incorporate the first five resonance pairs ($k = 0, 1, 2, 3, 4$) in the Hong-Ou-Mandel measurement. Different from the single Hong-Ou-Mandel dip in the degenerate single-resonance case, we observe the fast oscillation of the coincidence count due to the existence of multiple resonance pairs (Fig. 5c)[28]. The envelope of the Hong-Ou-Mandel interference pattern (green shaded area in Fig. 5c) is determined by the joint spectral-amplitude profiles of resonance pairs. With similar cavity linewidths and small dispersion, the joint spectral-amplitude of different resonance pairs have similar profiles. Therefore, the envelop of the coincidence count with five resonance pairs matches the single Hong-Ou-Mandel dip in the degenerate single-resonance case. Upon zoom-in of the coincidence pattern around zero time delay, narrow coincidence dips with high visibility can be observed, proving the intra-pair

phase coherence between symmetric resonances (Fig. 5d). We note that the Hong-Ou-Mandel experiment is not sufficient to prove the inter-pair coherence of QFCs. The complete characterization of coherence and entanglement in the frequency domain should be implemented with the superposition of different frequency modes using active methods such as nonlinear frequency mixing and electro-optic modulation[11,28,29]. We also observe the revival of the coincidence dips with a delay period of 1.4 ps, which agrees with the free-spectral range of the photonic ring cavity (362 GHz). When we zoom into the coincidence pattern around 1.1 ns delay time in Fig. 5c, we can still observe the revival of coincidence dips, but with a smaller visibility (Fig. 5e).

DISCUSSION
While the parallel processing of QFCs in the path domain does not require frequency operation, it is highly desired that coherent frequency operation can be realized on the same chip. Frequency
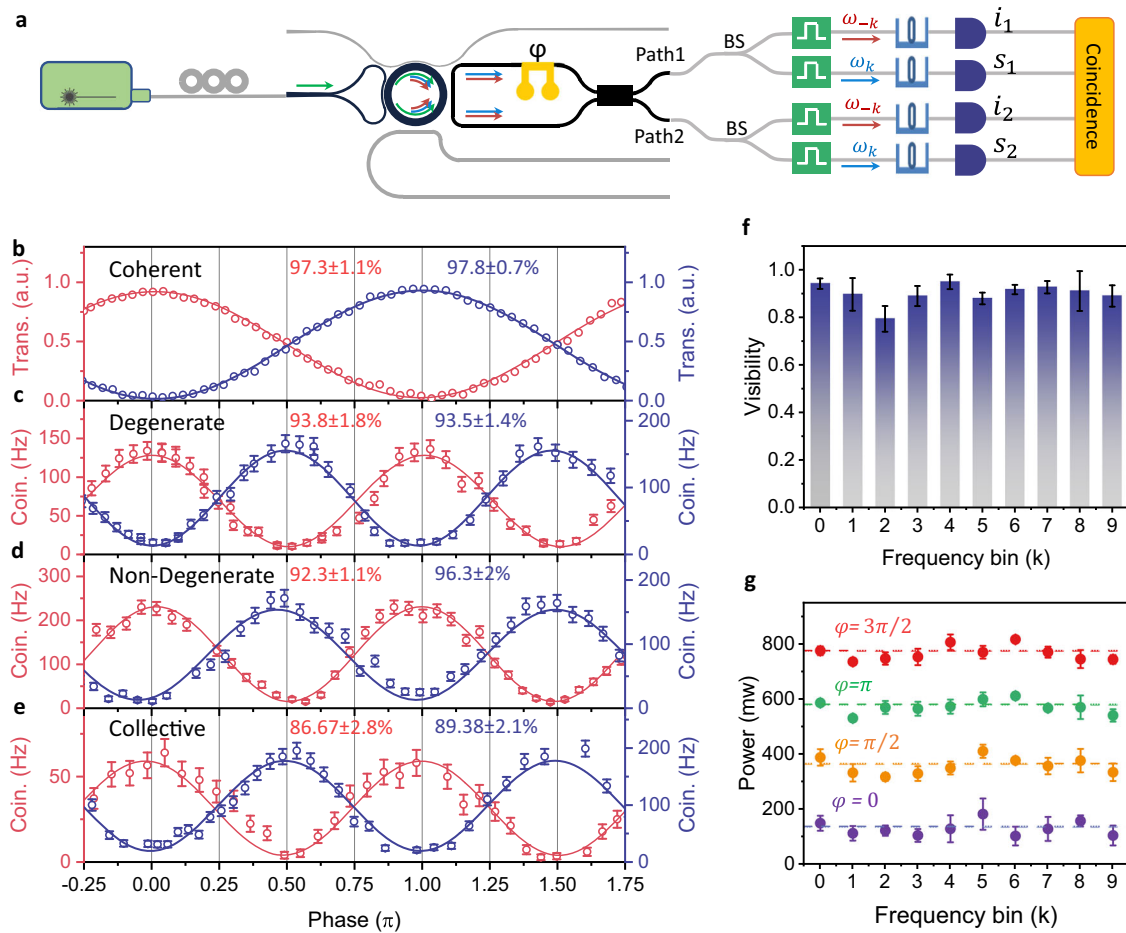
Fig. 3 On-chip parallel quantum processing. a Schematic of the measurement setup for parallel quantum interference of QFCs. **b** Transmission of the coherent light through a Mach-Zehnder interferometer (Supplementary Note III). **c, d** Correlation in the same path (red) and different paths (blue) of the degenerate resonance pair (**c**), non-degenerate resonance pair (**d**), and first five resonance pairs (**e**). Error bars of coincidence counts are estimated by assuming the Poisson distribution of photon counting. Error bars of visibility is estimated using the propagation of uncertainty in the maximum and minimum of coincidence counts. **f** The average visibility of correlations in the same path and in different paths with different resonance pairs. **g** Driving power of the thermal-optic phase shifter for different phases and resonance pairs. Error bars are obtained from the power variation in multiple measurements.

operation over QFCs have been realized with free-space and fiber-based components[11,28,30]. However, its demonstration with integrated photonics remains exclusive. Compared with QFC generation using SiN and Hydex glass[31], AlN holds great promise for on-chip frequency operation as the strong second-order nonlinearity can enable efficient phase modulation. This has been demonstrated using integrated AlN photonic devices with performance exceeding commercial fiber-based and free-space modulators[32]. With integrated programmable filters, arbitrary unitary transformation of frequency modes can be realized on chip[30,33–35], leading to the complete coherent manipulation of high-dimensional entanglement on chip using integrated second-order nonlinearity. In this work, Sagnac configuration is used to ensure the identical spectral distribution. However, the number of QFCs is limited to two. To further expand the dimension in the path domain, multiple ring cavities are required. In this case, spectral overlapping can be achieved with post-fabrication tuning of photonic ring cavities and quantum frequency conversion of QFCs.

In conclusion, we have demonstrated the parallel processing of QFCs with an integrated AlN platform. Parametric down-conversion in the Sagnac-configuration AlN ring cavity leads to the efficient generation of indistinguishable QFCs. We further present the simultaneous high-visibility quantum interference and

high-fidelity state control for different frequency modes in QFCs. We realize the deterministic separation of QFCs without spectral filtering. This leads to the demonstration of high-dimensional Hong-Ou-Mandel effect with integrated QFCs. Our work can significantly expand the dimension of quantum photonic systems while simultaneously enhancing quantum functionality, pushing the frontier for photonic quantum information processing.

METHODS

AlN wafer growth

The AlN wafer is grown on sapphire substrate with c-plane (0001) by MOCVD. Trimethylaluminum (TMA), ammonia (NH_3) and hydrogen (H_2) are used as the aluminum source, nitrogen source, and carrier gas, respectively. The growth started with a 25-nm low-temperature AlN buffer layer at 550 °C, followed by the growth of 1-μm high quality AlN layer at 1200 °C.

Device fabrication

The device is fabricated with 1-μm AlN film on sapphire grown by MOCVD. We use electron-beam lithography to exposure FOX-16 resist to define the photonic circuit. After development in
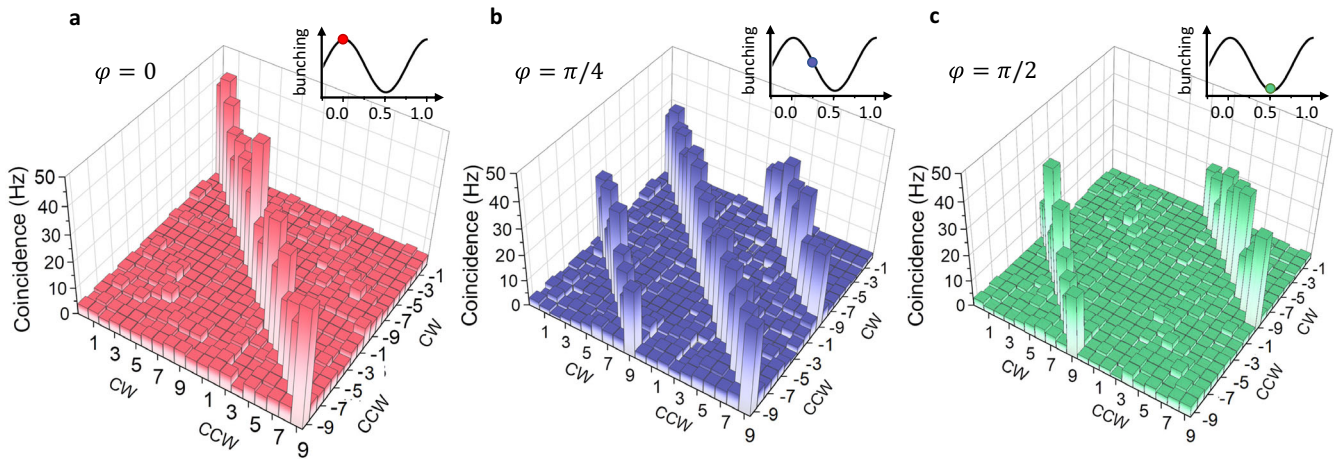
Fig. 4 Quantum state reconfiguration. Correlation matrix between different path and frequency modes under **a** bunching with $\varphi = 0$, **b** superposition with $\varphi = \pi/4$, and **c** anti-bunching with $\varphi = \pi/2$ conditions.
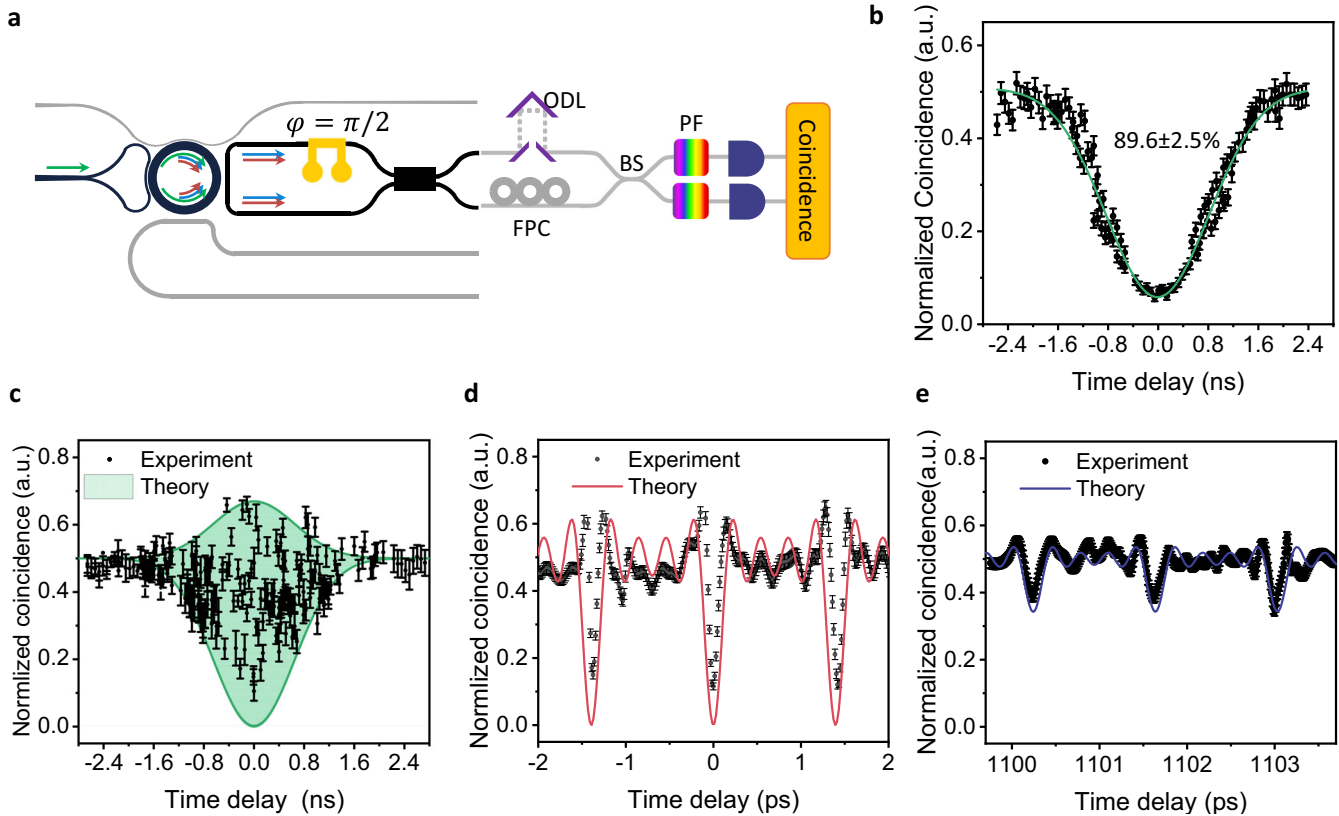

Fig. 5 High-dimensional quantum interference. a Schematic of the measurement setup for high-dimensional Hong-Ou-Mandel effect. ODL, optical delay line; BS: beamsplitter; PF: programmable filter. **b** Normalized coincidence rate between the two SNSPDs with photon pairs in the degenerate resonance. **c** Normalized coincidence rate between the two SNSPDs with photon pairs from first five resonance pairs. Theoretical envelop of the coincidence rate is also plotted. **d** Measured coincidence rate (black dot) and theoretical calculation (red) near zero time delay in (**c**). **e** Measured coincidence rate (black dot) and theoretical calculation (blue) at time delay around 1.1 ns in (**c**). Error bars are estimated by assuming the Poisson distribution of photon counting.

Tetramethylammonium hydroxide (TMAH), the pattern is transferred to AlN layer with reactive ion etching (RIE) using Cl_2/BCl_3/Ar chemistry. Then 2-μm SiO_2 is deposited by PECVD as the cladding layer. Finally, electrodes for phase shifter is defined with S1813 photoresist using photolithography, followed by Ti/Pt (5/200 nm) deposition and lift-off in Acetone.

DATA AVAILABILITY

REFERENCES

1. Collins, D., Gisin, N., Linden, N., Massar, S. & Popescu, S. Bell inequalities for arbitrarily high-dimensional systems. *Phys. Rev. Lett.* **88**, 040404 (2002).
2. Cerf, N. J., Bourennane, M., Karlsson, A. & Gisin, N. Security of quantum key distribution using d-level systems. *Phys. Rev. Lett.* **88**, 127902 (2002).
3. Lanyon, B. P. et al. Simplifying quantum logic using higher-dimensional hilbert spaces. *Nat. Phys.* **5**, 134–140 (2009).
4. Erhard, M., Krenn, M. & Zeilinger, A. Advances in high-dimensional quantum entanglement. *Nat. Rev. Phys.* **2**, 365–381 (2020).
5. Da Lio, B. et al. Path-encoded high-dimensional quantum communication over a 2-km multicore fiber. *npj Quantum Inf.* **7**, 1–6 (2021).
6. Leach, J. et al. Quantum correlations in optical angle–orbital angular momentum variables. *Science* **329**, 662–665 (2010).
7. Fickler, R. et al. Quantum entanglement of high angular momenta. *Science* **338**, 640–643 (2012).
8. Xie, Z. et al. Harnessing high-dimensional hyperentanglement through a biphoton frequency comb. *Nat. Photonics* **9**, 536–542 (2015).
9. Reimer, C. et al. Generation of multiphoton entangled quantum states by means of integrated frequency combs. *Science* **351**, 1176–1180 (2016).
10. Jaramillo-Villegas, J. A. et al. Persistent energy–time entanglement covering multiple resonances of an on-chip biphoton frequency comb. *Optica* **4**, 655–658 (2017).
11. Kues, M. et al. On-chip generation of high-dimensional entangled quantum states and their coherent control. *Nature* **546**, 622–626 (2017).
12. Cui, C., Zhang, L. & Fan, L. Photonic analog of mollow triplet with on-chip photon-pair generation in dressed modes. *Opt. Lett.* **46**, 4753–4756 (2021).
13. Walborn, S. P., Monken, C., Pádua, S. & Ribeiro, P. S. Spatial correlations in parametric down-conversion. *Phys. Rep.* **495**, 87–139 (2010).
14. Dada, A. C., Leach, J., Buller, G. S., Padgett, M. J. & Andersson, E. Experimental high-dimensional two-photon entanglement and violations of generalized bell inequalities. *Nat. Phys.* **7**, 677–680 (2011).
15. Edgar, M. P. et al. Imaging high-dimensional spatial entanglement with a camera. *Nat. Commun.* **3**, 1–6 (2012).
16. Marcikic, I. et al. Time-bin entangled qubits for quantum communication created by femtosecond pulses. *Phys. Rev. A.* **66**, 062308 (2002).
17. Vagniluca, I. et al. Efficient time-bin encoding for practical high-dimensional quantum key distribution. *Phys. Rev. A* **14**, 014051 (2020).
18. Mazeas, F. et al. High-quality photonic entanglement for wavelength-multiplexed quantum communication based on a silicon chip. *Opt. Express* **24**, 28731–28738 (2016).
19. Feng, L.-T. et al. Generation of a frequency-degenerate four-photon entangled state using a silicon nanowire. *npj Quantum Inf.* **5**, 90 (2019).
20. Guo, X. et al. Parametric down-conversion photon-pair source on a nanophotonic chip. *Light Sci. Appl.* **6**, 16249–16249 (2017).
21. Law, C., Walmsley, I. A. & Eberly, J. Continuous frequency entanglement: effective finite hilbert space and entropy control. *Phys. Rev. Lett.* **84**, 5304 (2000).
22. Fedorov, M. & Miklin, N. Schmidt modes and entanglement. *Contemp. Phys.* **55**, 94–109 (2014).
23. Luo, K.-H. et al. Direct generation of genuine single-longitudinal-mode narrow-band photon pairs. *N. J. Phys.* **17**, 073039 (2015).
24. Luo, K.-H., Herrmann, H. & Silberhorn, C. Temporal correlations of spectrally narrowband photon pair sources. *Quantum Sci. Technol.* **2**, 024002 (2017).
25. Myilswamy, K. V. et al. Time-resolved hanbury brown–twiss interferometry of on-chip biphoton frequency combs using vernier phase modulation. *Phys. Rev. Appl.* **19**, 034019 (2023).
26. Franson, J. Nonlocal cancellation of dispersion. *Phys. Rev. A* **45**, 3126 (1992).
27. Chen, J., Lee, K. F. & Kumar, P. Deterministic quantum splitter based on time-reversed hong-ou-mandel interference. *Phys. Rev. A* **76**, 031804 (2007).
28. Lingaraju, N. B. et al. Quantum frequency combs and hong–ou–mandel inter-ferometry: The role of spectral phase coherence. *Opt. Express* **27**, 38683–38697 (2019).
29. Lu, H.-H. et al. Bayesian tomography of high-dimensional on-chip biphoton fre-quency combs with randomized measurements. *Nat. Commun.* **13**, 4338 (2022).
30. Lukens, J. M. & Lougovski, P. Frequency-encoded photonic qubits for scalable quantum information processing. *Optica* **4**, 8–16 (2017).
31. Kues, M. et al. Quantum optical microcombs. *Nat. Photonics* **13**, 170–179 (2019).
32. Fan, L., Zou, C.-L., Zhu, N. & Tang, H. X. Spectrotemporal shaping of itinerant photons via distributed nanomechanics. *Nat. Photonics* **13**, 323–327 (2019).
33. Khan, M. H. et al. Ultrabroad-bandwidth arbitrary radiofrequency waveform generation with a silicon photonic chip-based spectral shaper. *Nat. Photonics* **4**, 117–122 (2010).
34. Cui, C., Seshadreesan, K. P., Guha, S. & Fan, L. High-dimensional frequency-encoded quantum information processing with passive photonics and time-resolving detection. *Phys. Rev. Lett.* **124**, 190502 (2020).
35. Shah, M. & Fan, L. Frequency superresolution with spectrotemporal shaping of photons. *Phys. Rev. Appl.* **15**, 034071 (2021).

AUTHOR CONTRIBUTIONS
The experiments were conceived by L.F. and C.C. The device was designed and fabricated by L.Z. and L.F. Measurements were performed by L.Z., L.F., and C.C. Analysis of the results was conducted by L.Z., L.F., and C.C. The AlN wafer was provided by J.Y., Y.G., and J.W. All authors participated in the manuscript preparation.

COMPETING INTERESTS
The authors declare no competing interests.

ADDITIONAL INFORMATION
Supplementary information The online version contains supplementary material available at https://doi.org/10.1038/s41534-023-00725-5.

Correspondence and requests for materials should be addressed to Linran Fan.

Reprints and permission information is available at http://www.nature.com/reprints

Publisher's note Springer Nature remains neutral with regard to jurisdictional claims in published maps and institutional affiliations.